CHEMISTRY OF MATERIALS

pubs.acs.org/cm

Article

Marinite $Li_2Ni(SO_4)_2$ as a New Member of the Bisulfate Family of High-Voltage Lithium Battery Cathodes

Shashwat Singh, Pawan Kumar Jha, Maxim Avdeev, Wenli Zhang, K. Jayanthi, Alexandra Navrotsky, Husam N. Alshareef, and Prabeer Barpanda*

Cite This: *Chem. Mater.* 2021, 33, 6108–6119

Read Online

ACCESS | Metrics & More | Article Recommendations | Supporting Information

ABSTRACT: Development of sustainable, economic, and high-voltage cathode materials forms the cornerstone of cathode design for Li-ion batteries. Sulfate chemistry offers a fertile ground to discover high-voltage cathode materials stemming from a high electronegativity-based inductive effect. Herein, we have discovered a new polymorph of high-voltage *m*-$Li_2Ni^{II}(SO_4)_2$ bisulfate using a scalable spray drying route. Neutron and synchrotron diffraction analysis revealed a monoclinic structure (s.g. $P2_1/c$, #14) built from corner-shared NiO_6 octahedra and SO_4 tetrahedra locating all Li^+ in a distinct site. Low-temperature magnetic susceptibility and neutron diffraction measurements confirmed long-range A-type antiferromagnetic ordering in *m*-$Li_2Ni^{II}(SO_4)_2$ below 15.2 K following the Goodenough–Kanamori–Anderson rule. *In situ* X-ray powder diffraction displayed an irreversible (monoclinic → orthorhombic) phase transformation at ∼400 °C. The *m*-$Li_2Ni^{II}(SO_4)_2$ framework offers two-dimensional Li^+ migration pathways as revealed by the bond valence site energy (BVSE) approach. The electronic structure obtained using first-principles (DFT) calculation shows a large electronic band gap (E_g ∼ 3.8 eV) with a trapped state near the Fermi energy level triggering polaronic conductivity. As per the DFT study, *m*-$Li_2Ni^{II}(SO_4)_2$ can work as a 5.5 V (vs Li^+/Li^0) cathode for Li-ion batteries, with suitable electrolytes, coupling both cationic ($Ni^{II/III}$) and anionic (O^-) redox activity.

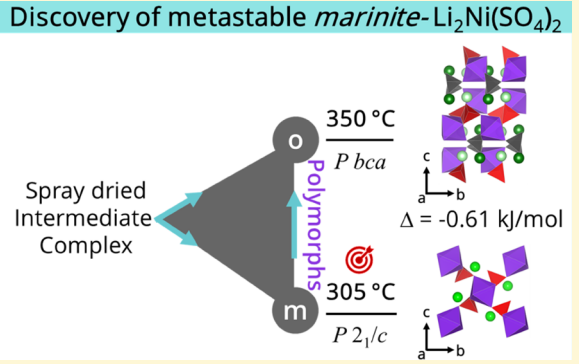

INTRODUCTION

Since their commercial debut in 1991, Li-ion batteries (LIBs) continue to dominate the consumer electronics sector along with (hybrid) automobiles and grid storage domains. For battery development, we need to consider electrochemical performance, cycle life, materials/process cost, safety, and sustainability. Some applications (e.g., microgrid storage) can be implemented with low-cost batteries with moderate energy density. However, true grid-scale systems require the development of new battery insertion materials to achieve higher energy densities at much lower costs. In this context, polyanionic compounds form a treasure house of materials exhibiting rich crystal chemistry, polymorphism, tunable voltage, and chemical/thermal stability. Insertion materials with polyanionic units $[(XO_4)_m^{n-}$: X = P, Si, Ti, V, Mo, etc.] have been explored over the last three decades based on the concept of inductive effect,[1,2] which has most significantly led to the discovery and commercialization of $LiFePO_4$.[3] The success of $LiFePO_4$ ushered in extensive research activity on various families of polyanionic cathodes such as borates ($LiMBO_3$), pyrophosphates ($Li_{2-x}MP_2O_7$), fluorophosphates ($Li_{2-x}MPO_4F$), and silicates (Li_2MSiO_4).[4−7] As per Pauling's electronegativity values,[8] SO_4-based polyanionic systems can exhibit the highest redox potential. Indeed, various sulfate cathodes, such as fluorosulfate ($AMSO_4F$: A = Li, Na, K) and polysulfate $[A_2M_2(SO_4)_3]$ polymorphs, exhibit the highest Fe^{3+}/Fe^{2+} redox activity in Li-ion (ca. 3.9 V), Na-ion (ca. 3.8 V), and K-ion (ca. 3.7 V) batteries.[9−13]

Bisulfates form one such SO_4-based high-voltage polyanionic cathodes, kick-started by monoclinic $Li_2Fe(SO_4)_2$ with a redox potential of 3.83 V (vs Li^+/Li^0).[14] Later, the bisulfate family was successfully extended to other transition metal homologues $Li_2M(SO_4)_2$ (M = Mn, Co, Ni, and Zn) stabilizing in either the monoclinic (*m*-$P2_1/c$) marinite phase or the orthorhombic (*o*-*Pbca*) phase. Among these compounds, Zn-analogue $Li_2Zn(SO_4)_2$ was an exception showing thermally induced irreversible phase transformation between *o* and *m* phases. High entropy, induced in the material from reactive ball-milling, typically favored the growth of the denser (metastable) *o*-polymorph. This route could only stabilize one of the two possible polymorphs: *m*-phase (M = Mn) and

Received: May 15, 2021
Revised: July 6, 2021
Published: July 30, 2021

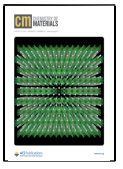

https://doi.org/10.1021/acs.chemmater.1c01669
Chem. Mater. 2021, 33, 6108–6119

o-phase (M = Mg, Fe, Co, Zn, and Ni).[15] For both polymorphs, the positive enthalpy of formation decreased with an increase in the ionic radius of the transition metal center, except for Ni-analogues.[16] Thermal treatment of such compounds resulted in polymorphic transformation barring Mn- and Ni-based phases. On the electrochemistry front, the *o*-polymorph showed better electrochemical properties than *m*-$Li_2Fe(SO_4)_2$, with lower overpotential upon Li (de)insertion with a staircase-like galvanostatic profile having plateaus at 3.73 and 3.85 V. The presence of a $T_M-O-O-T_M$ link allowed for the super-superexchange magnetic interaction in the bisulfate $Li_2M(SO_4)_2$ structure working as a model case for the Goodenough–Kanamori–Anderson rule. Subsequently, the magnetic property and the ground-state magnetic structure of the *m*-phase (Mn, Fe, Co) and *o*-phases (Fe, Co, Ni) were reported.[17−19] The above studies underscore the importance of polymorphism and synthesis routes in insertion host discovery. They motivate further exploration of bimetallic sulfates to unravel rich crystal chemistry suitable for secondary batteries.

While the *o*-phase of $Li_2Ni(SO_4)_2$ has a comparable heat of formation to the *m*-phase of Mn- and Co-analogues,[16] there is no report on the monoclinic polymorph of $Li_2Ni(SO_4)_2$ with attempts involving solid-state and reacting ball-milling process routes. Deviating from conventional methods, sulfate cathodes can be produced via two-step soft chemical aqueous routes such as spray drying, whose salient features include intimate atom-level mixing, scalability, and energy-savvy synthesis with restricted annealing duration.[20] The present work employs the spray drying method to unravel hitherto-unknown monoclinic marinite $Li_2Ni(SO_4)_2$ bisulfate that transforms to an orthorhombic polymorph upon heating. Synergizing experimental and computational tools, the Li^+ diffusion pathways, optical/electronic band gap, crystal/magnetic structure, and the thermochemical properties of this novel marinite $Li_2Ni(SO_4)_2$ are elucidated. With suitable electrolytes, this Ni-analogue can work as a potential high-voltage (ca. 5.5 V vs Li/Li^+) cathode for Li-ion batteries.

EXPERIMENTAL SECTION

Material Synthesis. The spray drying synthesis (SDS) of the metastable $Li_2Ni(SO_4)_2$ phase was carried out using a Büchi B-90 spray dryer by feeding a uniform aqueous solution containing stoichiometric amounts of hydrated precursors ($Li_2SO_4·H_2O$ and $NiSO_4·6H_2O$). Compared to the solid-state route, the presence of liquid media ensured atomic-level mixing and easy ionic diffusion.[21] Small droplets were produced from a piezoelectric-driven spray head with a thin vibrating perforated mesh. These droplets interacted with hot air while descending the chamber with the inlet and outlet temperatures fixed at 220 and 80 °C, respectively, ensuring quick solvent evaporation to form an intermediate complex. This spray-dried (intermediate) powder was collected at the bottom using an electrostatic particle collector for submicron and nanometric particles and a cyclone separator for micron-sized particles. Then, this intermediate complex was pelletized and annealed in the temperature range of 250−420 °C for 12−24 h (in air). In this SDS route, the low temperature and the time of annealing were expected to yield particles with minimal coarsening and grain growth, beneficial for the final electrode performance. To gauge phase formation and the possible phase transformation upon heating, a small amount (10−20 mg) of the intermediate powder was subjected to simultaneous thermal analysis (STA-8000) in the temperature range of RT−500 °C (heating rate = 10 °C/min) under a steady N_2 atmosphere.

Structural and Physical Characterization. Powder X-ray diffraction (PXRD) patterns of pristine samples were acquired using a PANalytical Empyrean X-ray diffractometer (PANalytical, Malvern, U.K.) equipped with a Cu Kα source (λ_1 = 1.5405 Å, λ_2 = 1.5443 Å, operating at 40 kV/30 mA). Typical PXRD patterns were collected in Bragg−Brentano geometry in the 2θ range of 10−90° with a step size of 0.026°. The crystal structure and the phase analyses were conducted by Rietveld refinement using GSAS-I software with EXPGUI as its graphical user interface.[22−24] A suite of parameters, background, scale factor, zero shift, lattice parameters, profile function, and phase parameters, were systematically and iteratively refined. Structure illustration was performed using VESTA software.[25] Phase transformation in the $Li_2Ni(SO_4)_2$ system was probed using *in situ* high-temperature XRD measurement (Bruker D8 Advance, Cu source) in the temperature range of 30−500 °C with an interval of 20 °C.

The morphology was observed using a Carl Zeiss Ultra55 field emission scanning electron microscope (FESEM) with a thermal field emission-type tungsten source operating in the range of 0.1−30 kV. To avoid charging, an electronically conductive path was provided by gold-sputtering the powder samples cast over a double-sided carbon tape. The spatial elemental distribution was examined at 10 kV in both line scan and area scan modes using an energy-selective backscattered (EsB) detector. A transmission electron microscope (TEM) Titan Themis (Thermo-FEI, operating at 300 kV) was used to acquire the selected area electron diffraction (SAED) pattern and high-resolution transmission electron microscopy (HRTEM) images. For transmission electron microscopy, the powder sample was dispersed in anhydrous ethanol, followed by drop-casting on holey carbon−copper grids and drying under an infrared lamp.

The temperature dependence of magnetization was measured using a physical property measurement system (PPMS) (Quantum Design) under a constant external magnetic field of 10 kOe in zero-field-cooled (ZFC) and field-cooled (FC) modes between 2 and 300 K. The powder sample enclosed in a thin Teflon tape was used as a specimen for the measurement.

Neutron Pattern Diffraction Analysis. Neutron powder diffraction (NPD) data were collected on the high-resolution diffractometer Echidna[26] at the OPAL facility (Lucas Heights, Australia) at room temperature using neutrons of wavelength 1.6215 Å. Low-temperature NPD patterns (down to 3 K) were acquired using neutrons of wavelength 2.4395 Å. For the NPD measurements, ∼3 g of the powder sample was loaded into a 9 mm diameter cylindrical vanadium can placed inside a closed-cycle refrigerator. Rietveld analysis of the data was performed using the Fullprof Suite with the default neutron scattering lengths and the Ni^{2+} magnetic form factor.[27]

Optical Properties. The Fourier transform infrared (FTIR) (PerkinElmer) spectrum was collected in universal attenuated total reflectance (UATR) mode over the spectral range of 4000−650 cm^{-1}. The diffused reflectance mode of UV−vis−NIR spectroscopy was used to acquire reflectance data of each powder sample using a Shimadzu MPC3600 instrument covering a broad wavelength region (200−2500 nm). The simplified Kubelka−Munk theory was followed to estimate the optical band gaps of the two polymorphs of $Li_2Ni(SO_4)_2$. The obtained spectra were treated with the Kubelka−Munk function $f(R) = \frac{(1-R)^2}{2R} = \frac{K}{s}$, where R is the reflectance, K is the absorption coefficient, and s is the scattering coefficient.[28] Finally, the graph of $[f(R)\cdot h\nu]^n$ vs energy ($h\nu$) was plotted, where n was varied between 0.5 and 2 for the indirect and direct gap, respectively.[29]

Thermochemistry Study. PXRD and TG-DSC measurements were performed before and after the calorimetric measurement to detect any possible decomposition and check for adsorbed water on the sample due to exposure in the ambient atmosphere prior to calorimetric experiments. Dissolution enthalpy of *m*-$Li_2Ni(SO_4)_2$ was measured using both CSC 4400 isothermal (with IMC data acquisition software) and Hart Scientific (with Labview software) microcalorimeters with mechanical stirring of the samples and reagents at 25 °C.[30] The calorimeters were calibrated with KCl (NIST standard reference material) by dissolving 15 mg pellets in 25 g of water at 25 °C. The solution enthalpy of this reference concentration (0.008 mol kg^{-1}), deduced from the literature and the

https://doi.org/10.1021/acs.chemmater.1c01669
Chem. Mater. 2021, 33, 6108−6119

enthalpy of dilution measurements,[31] was used to obtain the calorimeter calibration factor.

In a typical calorimetric run, 6−7 mg of the sample was pressed into a pellet and then dropped into 25 g of 5 M HCl placed in the calorimeter. All samples were dissolved in 5 N HCl to form dilute solutions containing dissolved lithium, nickel, and sulfate ions. The integrated area under the recorded microwatt signal relative to a linear baseline corresponds to the total heat effect. An appropriate thermochemical cycle based on Hess' law (difference in the heat of solution of products and reactants) was used to calculate the enthalpy of formation (see Table 4).

Computational Methods. The Li^+ diffusion pathways in $Li_2Ni(SO_4)_2$ polymorphs were calculated using the computationally economic bond valence site energy (BVSE) method[32,33] implemented in the softBV program. The BVSE method calculates the energy of the possible positions of the mobile ions in the 3D framework as a function of their mismatch ($|\Delta V|$) in bond valence ($s_{Li\text{-}X}$) estimated using the empirical bond valence sum model. Connecting the low-valence-site-energy E_{BVSE} positions of the mobile ion (Li^+) forms the diffusion pathways. E_{BVSE}(Li) was calculated using grids spanning the structure model with a resolution of (0.1 Å)^3. The first-principles electronic structure calculations, based on density functional theory (DFT), aided in predicting the band gap and the (de)lithiation voltage of m-$Li_2Ni(SO_4)_2$. The DFT calculation was performed using the projector augmented wave (PAW) method implemented in the Vienna *Ab initio* Simulation Package (VASP).[34,35] The self-interaction error of standard DFT was compensated using the generalized gradient approximation GGA + U framework,[36,37] where $U_{eff}(U - J)$ was taken as 6.2 eV. The force convergence limit was fixed at 0.01 eV/Å, with the Γ-centered Monkhorst−Pack k-point mesh having a 48 Å density as the Brillouin zone sampling criterion, and the plane wave cutoff was set at 520 eV.

RESULTS

Synthesis and Structure. For the battery community, Ni-based analogues remain a challenge from the synthesis and electrochemistry points of view. While appealing for high-voltage operation, these Ni-based analogues often suffer from difficulty in the synthesis of pure phase, material instability, and poor activity. While the Tarascon group has reported polymorphs of $Li_2M(SO_4)_2$ (M = Fe, Co) by mechanical-milling and solid-state routes, they concluded that $Li_2Ni(SO_4)_2$ exists only in the orthorhombic phase.[15] As metastable (low-temperature) polymorphs often provide exciting electrochemical properties, we attempted the synthesis of the metastable monoclinic Ni-analogue. Our main strategy was to use the soft chemistry technique involving low energy, as a high-energy process invariably leads to a thermodynamically stable and more symmetric orthorhombic phase. Deviating from energy/pressure-intensive solid-state/mechanical-milling routes, we have employed the two-step spray drying synthesis (SDS). SDS facilitates intimate atomic-level mixing of precursors in aqueous solution and formation of complexation to yield an intermediate product, which can easily convert to the final product with milder annealing (i.e., lower annealing temperature and/or duration). SDS is easily scalable and is already used on a large scale in ceramic tile manufacturing industries.[38] On another note, over the last few decades, the successful synthesis of various SO_4-based cathodes (bisulfates, fluorosulfates, etc.) has been attributed to the formation of pure monohydrate ($MSO_4{\cdot}H_2O$) and anhydrous (MSO_4) precursors, making the entire process cumbersome. In contrast, SDS can directly employ commercially available polyhydrate ($MSO_4{\cdot}nH_2O$, n = 6, 7) precursors and involves *in situ* dehydration and product formation.

Spray drying of the precursor solution led to an intermediate crystalline product having a minor amount of unreacted $NiSO_4{\cdot}6H_2O$ precursor (Figure S1). Simultaneous thermal analysis, combining thermogravimetric analysis (TGA) and differential scanning calorimetry (DSC), of this intermediate phase was conducted in a steady N_2 flow (RT−500 °C). Following initial endothermic peaks corresponding to dehydration (up to 200 °C), endothermic (#crest) and exothermic (*trough) peaks at 270 and 410 °C appeared, hinting at formation of the metastable monoclinic $Li_2Ni(SO_4)_2$ phase, followed by its transformation to the orthorhombic polymorph (Figure S2).[16] This phase transformation was found to be irreversible with a rerun of DSC measurement. The synthesized material was stable up to 500 °C. Taking a clue from the DSC study, the intermediate compound was annealed at 300−350 °C (in air) for 10−12 h to obtain the target marinite m-$Li_2Ni(SO_4)_2$ product having an ivory-white appearance. Rietveld analysis was carried out on the neutron diffraction pattern (NPD) of m-$Li_2Ni(SO_4)_2$ collected at room temperature (λ = 1.6215 Å, ECHIDNA beamline, ANSTO, Australia) as shown in Figure 1a. It was modeled with a

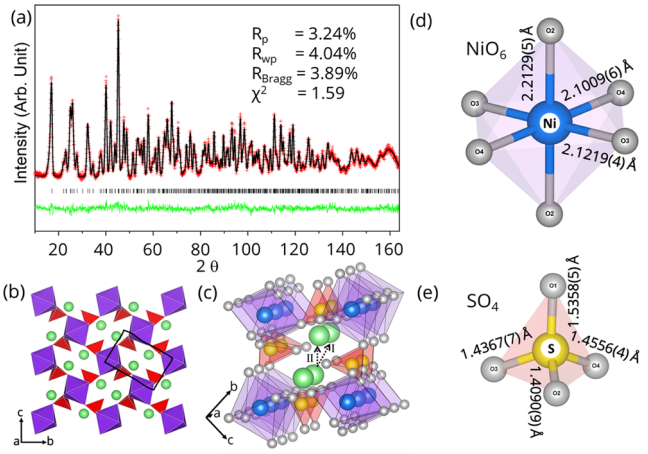

Figure 1. (a) Rietveld refined neutron diffraction (NPD) pattern of m-$Li_2Ni(SO_4)_2$ collected at room temperature (λ = 1.6215 Å). The red crosses and the black and green solid lines indicate the observed and calculated patterns and their difference, respectively. The tick marks indicate the Bragg diffraction peaks. (b) Structural illustration of m-$Li_2Ni(SO_4)_2$ (s.g. $P2_1/c$) projected along the a-axis. Li atoms, NiO_6 octahedra, and SO_4 tetrahedra are represented in green, violet, and red, respectively. (c) Illustration of the tunnel along the [100] direction housing Li at symmetrically equivalent positions pointed by the free corner (O1) of sulfate tetrahedra. Li−Li jump expected to occur in a combination of Paths I and II. Bond lengths estimated from Rietveld analysis are depicted for (d) NiO_6 octahedra and (e) SO_4 tetrahedra.

monoclinic framework ($P2_1/c$ #14 symmetry) with lattice parameters a = 4.9646(2) Å, b = 8.0166(3) Å, c = 8.7312(4), and β = 121.8804(10)° and unit cell volume = 295.08(2) Å^3. The lattice parameters and unit cell volume follow a linear decreasing trend in the m-$Li_2M(SO_4)_2$ family and are expectedly lower than those of m-$Li_2Co(SO_4)_2$ owing to the small cationic size of Ni.[15] The details of the crystallographic parameters are listed in Table 1.

The corresponding crystal structure is illustrated in Figure 1b−e. In the framework of marinite m-$Li_2Ni(SO_4)_2$ built with NiO_6 octahedra and SO_4 tetrahedra, all corners of $[NiO_6]^{10-}$ octahedra are connected to sulfate $[SO_4]^2$ tetrahedra in a pin-

https://doi.org/10.1021/acs.chemmater.1c01669
Chem. Mater. 2021, 33, 6108−6119

Table 1. Crystallographic Data for m-$Li_2Ni(SO_4)_2$ Obtained from Rietveld Analysis of Neutron Powder Diffraction Data (λ = 1.6215 Å) Collected at Room Temperature

formula [molecular weight]	$Li_2Ni(SO_4)_2$ [264.70]
crystal system	monoclinic
space group	$P2_1/c$ (#14)
unit cell parameter (Å)	a = 4.9646(2), b = 8.0166(3), c = 8.7312(4), β = 121.8804(10)°, Z = 4
unit cell volume (Å^3)	295.08(2)
theoretical density (g cm^{-3})	2.977
reliability factors and goodness of fit values	R_p = 3.24%, R_{wp} = 4.04%, χ^2 = 1.59

atom	Wyckoff position	x	y	z	U_{iso} (Å^2)	bond valence sum (BVS)
Ni1	2a	0	0	0	0.0095(4)	1.85(1)
Li1	4e	0.0130(16)	0.6347(9)	0.1026(10)	0.0113(13)	1.21(1)
S1	4e	0.3375(9)	0.3066(6)	0.3052(6)	0.0085(10)	6.00(4)
O1	4e	0.1839(5)	0.4205(3)	0.1516(3)	0.0109(5)	2.17(2)
O2	4e	0.2080(5)	0.1347(3)	0.2485(3)	0.0104(5)	1.89(2)
O3	4e	0.2807(5)	0.3527(3)	0.4488(3)	0.0104(6)	2.01(3)
O4	4e	0.6819(5)	0.3025(3)	0.3796(3)	0.0107(5)	2.07(2)

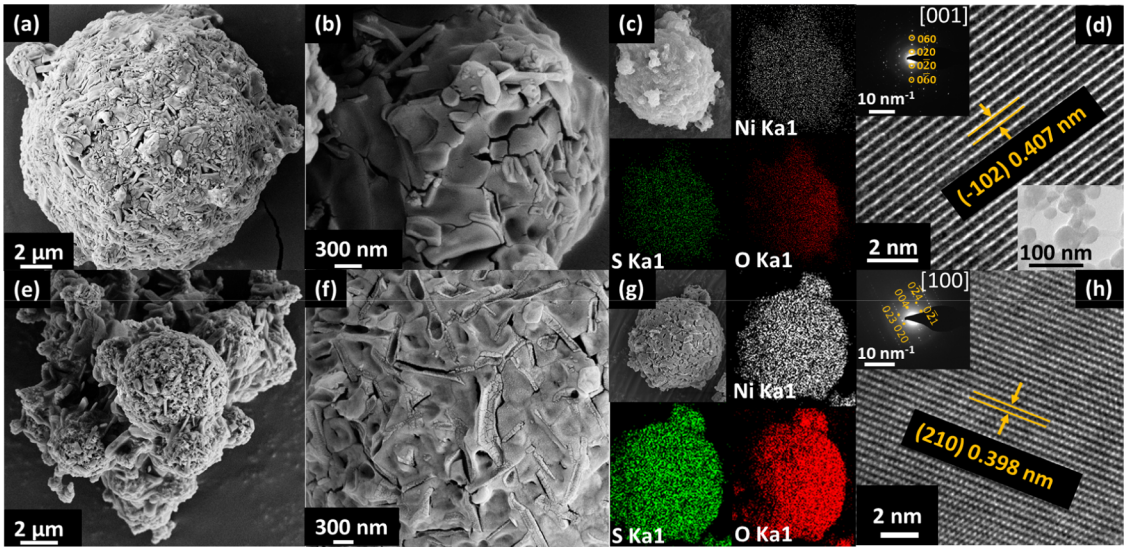

Figure 2. Morphology of (a–d) m-$Li_2Ni(SO_4)_2$ and (e, f) o-$Li_2Ni(SO_4)_2$ bisulfate polymorphs obtained from the spray drying route. (a, b) and (e, f) Representative secondary electron micrographs of spherical agglomerates with embedded finer nanoscale particles. (c) and (g) Elemental mapping with a homogeneous distribution of Ni (white), S (green), and O (red). (d) and (h) Corresponding HRTEM images and SAED patterns (inset) affirming the crystalline nature.

wheel fashion (Figure 1b). Conversely, three out of four corners of sulfate tetrahedra are connected to different $[NiO_6]^{10-}$ octahedra. The free SO_4 corner points to the channel running along [100], accommodating all constituent Li^+ ions in a distinct crystallographic site. Two adjacent Li^+ ions are separated by 4.965(62) Å along [100], whereas two rows of Li^+ ions are 2.757(61) Å apart. As per an earlier report on the marinite m-$Li_2M(SO_4)_2$ family, the thermodynamically favorable Li–Li jump may occur along Paths I and II (Figure 1c),[39] contained in a 1D tunnel running along the [100] direction. The NiO_6 octahedra are built with three distinct oxygen (denoted as O2, O3, and O4), where O3 and O4 form the equatorial plane while two O2 are at longitudinal ends (Figure 1d) with the axial Ni–O2 bond slightly longer than the equatorial bonds. The SO_4 tetrahedra have four distinct oxygen atoms, viz., O1, O2, O3, and O4, where O1 occupies the unshared corner (Figure 1e). Polyhedral information, bond distance, Baur's distortion index, and bond angle variance of NiO_6 octahedra and SO_4 tetrahedra for m-$Li_2Ni(SO_4)_2$ are compiled in Table S1.

The spray drying route can be easily extended to other analogues of the $Li_2M(SO_4)_2$ family, as well as their polymorphs. By simply annealing the intermediate product at a higher temperature (>350 °C), the orthorhombic polymorph o-$Li_2Ni(SO_4)_2$ was obtained. Rietveld analysis on XRD patterns and the detailed crystallographic parameters of m-$Li_2Ni(SO_4)_2$ and o-$Li_2Ni(SO_4)_2$ polymorphs are presented in Figure S3 and Tables S2 and S3. The structure and polyhedral information (ca. bond distance, Baur's distortion index, and bond angle variance) for the o-$Li_2Ni(SO_4)_2$ polymorph are compiled in Figure S3 and Table S4, in sync with an earlier report.[19] A signature feature of spray drying is the formation of spherical particles arising from spherical water droplets upon nebulization (acting as nanoreactors), followed by rapid dehydration in the spray drying chamber.[20] Spherical nanometric particles tend to agglomerate to form porous microspheres.[21] Indeed, spherical primary particles were observed for spray-dried m-$Li_2Ni(SO_4)_2$ and o-$Li_2Ni(SO_4)_2$ polymorphs (Figure 2). EDS mapping confirmed homogenous elemental distribution in the particles (Figure 2c,g). Representative

https://doi.org/10.1021/acs.chemmater.1c01669
Chem. Mater. 2021, 33, 6108–6119

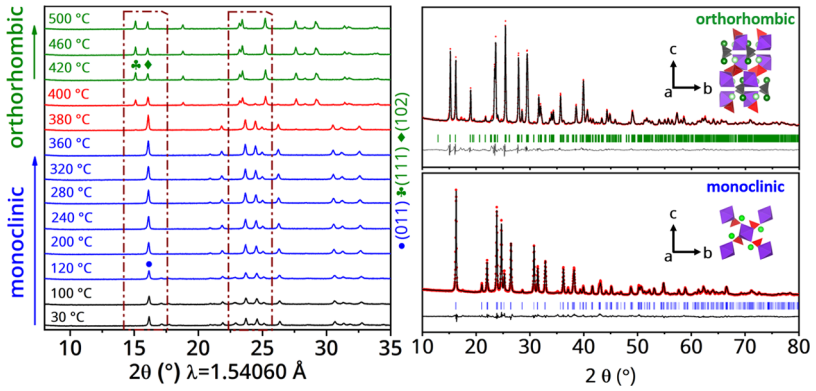

Figure 3. (Left) *In situ* high-temperature (30−500 °C) powder X-ray diffraction patterns of the spray-dried intermediate complex showing the monoclinic to orthorhombic phase transition in $Li_2Ni(SO_4)_2$. The blue, red, and green patterns correspond to the *m*-phase, the two-phase region, and the *o*-phase, respectively. (Right) Rietveld refinement of (bottom panel) marinite *m*-$Li_2Ni(SO_4)_2$ ($P2_1/c$, R_p = 2.65%, R_{wp} = 3.63%, χ^2 = 15.6) and (top panel) orthorhombic *o*-$Li_2Ni(SO_4)_2$ (*Pbca*, R_p = 2.8%, R_{wp} = 4.07%, χ^2 = 19.44). Red spheres, the black solid line, and blue/green vertical bars represent observed data, calculated profile, and reference positions, respectively. The inset shows the respective crystal structures.

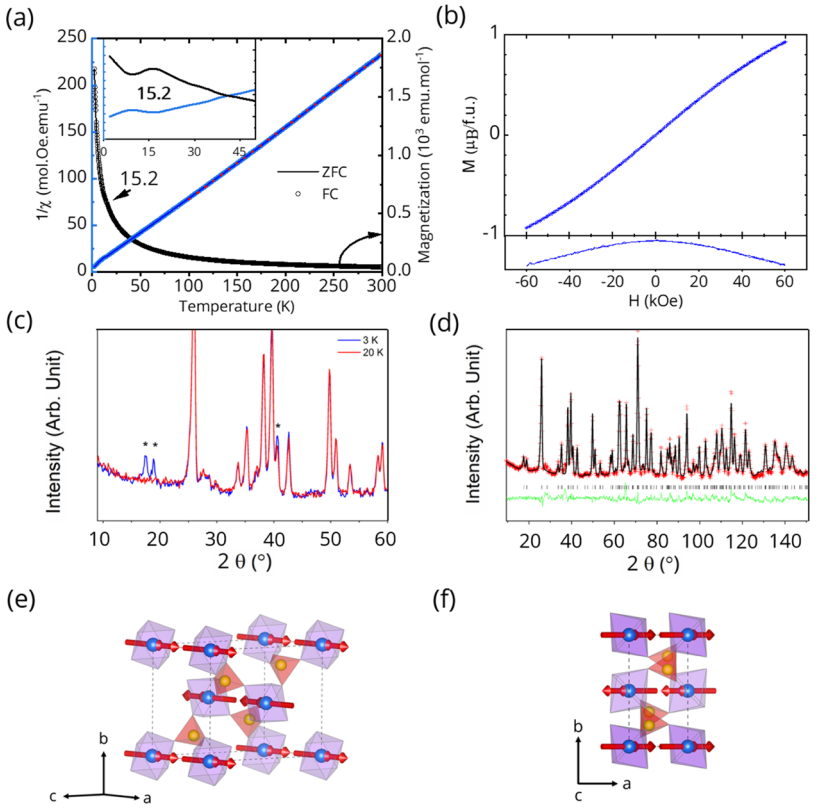

Figure 4. (a) Temperature-dependent magnetization curve of *m*-$Li_2Ni(SO_4)_2$ measured in zero-field-cooled (ZFC, black solid line) and field-cooled (FC, black circles) modes at 10 000 Oe between 2 and 300 K. The corresponding inverse magnetic susceptibility (light blue circles and line) vs temperature plot reveals an inflection at 15.2 K related to antiferromagnetic ordering. Curie−Weiss behavior is ascertained by linear fitting in the paramagnetic region in the temperature range of 200−300 K, shown by the red dashed line. (b) Magnetization (M vs H) curve of the title compound recorded at 6 K, showing no sign of ferromagnetic hysteresis. (c) NPD patterns collected at 3 K (blue) and 20 K (red). Asterisks emphasize the magnetic diffraction peaks. (d) Rietveld plot for the *m*-$Li_2Ni(SO_4)_2$ NPD data collected at 3 K (λ = 2.4395 Å). The red crosses and black and green solid lines indicate the observed and calculated patterns and their difference, respectively. The black tick marks indicate the position of the diffraction peaks. R_p = 3.65%, R_{wp} = 4.90%, R_{Bragg} = 7.79%, R_{mag} = 13.1%, and χ^2 = 4.59. (e, f) Magnetic structure of *m*-$Li_2Ni(SO_4)_2$ derived from the neutron powder diffraction data collected at 3 K with the magnetic space group $P2_1/c$ (#14.75), M_x = 2.3(1) μ_B. Light pink and light red polyhedra represent the NiO_6 octahedra and SO_4 tetrahedra, respectively. The blue spheres represent Ni atoms and the red arrows indicate the direction of the effective magnetic moment.

HRTEM images (Figure 2d, inset) revealed nanometric (~50 nm) particles, while SAED patterns and lattice fringes further reiterated the crystallinity of the target products (Figure 2d,h). Overall, micrometric agglomerates with a porous morphology were observed, which may facilitate electrolyte wetting that is favorable for the final cathode activity.

The thermal stability of the novel marinite *m*-$Li_2Ni(SO_4)_2$ was investigated using an *in situ* high-temperature XRD study

https://doi.org/10.1021/acs.chemmater.1c01669
Chem. Mater. 2021, 33, 6108−6119

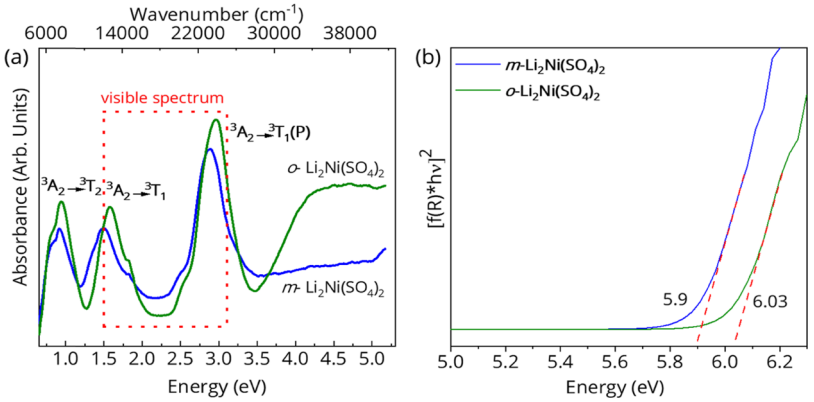

Figure 5. (a) UV−visible absorption spectra of the *m*- and the *o*-phase of $Li_2Ni(SO_4)_2$. Various d−d-transitions observed in both polymorphs have been indicated. Blue and green curves denote the *m*-phase and the *o*-phase, respectively. (b) Optical band gaps for two polymorphs of $Li_2Ni(SO_4)_2$ calculated using Kubelka−Munk functions (n = 2) applied to UV−vis spectra. Blue and green curves denote the *m*-phase and the *o*-phase, respectively.

in the temperature range of 30−500 °C with a step of 20 °C (Figure 3). The initial intermediate complex powder slowly transformed into the monoclinic phase on heating up to 360 °C, as indicated by the growth of the characteristic (011) peak of *m*-$Li_2Ni(SO_4)_2$ (at 2θ = 16.3°). Between 320 and 360 °C, the pure *m*-phase was identified. Upon further heating, from 380 °C onward, the intensity of the (011) peak decreased along with the appearance of a new (111) peak (2θ = 15.25°), the signature of *o*-polymorph. This (111) peak was accompanied by the (102) peak (2θ = 16.25°), replacing the (011) peak of the parent *m*-phase. From 420 °C onward, phase-pure orthorhombic polymorph *o*-$Li_2Ni(SO_4)_2$ was noticed. Rietveld refined XRD plots of the two polymorphs of $Li_2Ni(SO_4)_2$ are presented in Figure 3 (right). It confirms thermally induced phase transformation/polymorphism in monoclinic $Li_2Ni(SO_4)_2$. In congruence with the DSC study (Figure S2), this phase transformation was found to be irreversible in nature, once again indicating higher thermodynamic stability of the orthorhombic polymorph.

Magnetic Structure and Properties. Transition metal-based battery insertion materials, with their structural diversity, can provide interesting magnetic properties. The magnetic susceptibility of *m*-$Li_2Ni(SO_4)_2$ was measured in the temperature range of 2−300 K at 10 K Oe in both ZFC and FC modes as shown in Figure 4a. An inflection corresponding to long-range antiferromagnetic (AFM) ordering occurs below ∼15 K (Néel temperature, T_N) (Figure S5), which is lower than the T_N of *o*-polymorph (∼28 K).[19] For the bisulfate marinite [*m*-$Li_2M(SO_4)_2$] family, T_N follows an increasing trend [∼6 K (Fe) < ∼7 K (Co) < ∼15 K (Ni)]. A similar trend has been reported for the sulfate-based alluaudite family of high-voltage sodium battery cathodes.[40] The inverse magnetic susceptibility (χ^{-1}) was linearly fitted in the paramagnetic region (100−300 K) with the Curie−Weiss law $\chi = C/(T - \theta_{CW})$, which yielded the Curie constant C = 1.29 emu K mol^{-1}. The effective magnetic moment was calculated to be μ_{eff} = 3.21 μ_B per formula unit, where $\mu_{eff} \approx \sqrt{8 \times C}$ = 3.19 μ_B, slightly higher than the theoretical spin-only value for d^8 S = 1 Ni^{2+}, which suggests a partially quenched angular momentum contribution. The magnetization curve (M vs H) at 6 K displays an *S*-curve devoid of hysteresis, indicative of AFM ordering below ∼15 K (Figure 4b). The AFM behavior can theoretically stem from super-superexchange interactions due to the $Ni^{II}-O^{II-}-O^{II-}-Ni^{II}$ links present in the crystal structure of *m*-$Li_2Ni(SO_4)_2$, a model case of the Good-enough−Kanamori−Anderson rule. Following, low-temperature neutron powder diffraction (NPD) patterns of the *m*-$Li_2Ni(SO_4)_2$ sample were collected around the Néel temperature. The NPD data collected at 20 K could be successfully described using the same monoclinic $P2_1/c$ model framework as that used for the ambient condition (Figure S6 and Table S5).

The NPD data collected at 3 K clearly showed additional magnetic diffraction peaks, indicative of the long-range magnetic ordering (Figure 4c). All of the diffraction peaks of magnetic origin could be indexed by the crystallographic unit cell with the propagation vector k(0, 0, 0). Two compatible magnetic space groups, $P2_1/c$ (#14.75) and $P2_1'/c'$ (#14.79), were identified using the ISOTROPY Software Suite,[41] in agreement with the symmetry analysis for the isostructural Mn- and Co-analogues reported previously.[17] The $P2_1/c$ (#14.75) magnetic space group was found to be consistent with the experimental data. Moreover, although this magnetic space group allows for components of magnetic moments along all axes of the unit cell, examination of the data revealed no intensity associated with the components along *b*- and *c*-axes, and therefore only the component along the *a*-axis was further refined (Figure 4d). The value of the magnetic moment from NPD analysis at 3 K is 2.3(1) μ_B, which is consistent with the expected value of 2μ_B (for S=1, d^8 Ni^{2+}) estimated from the inverse susceptibility vs temperature plot. The magnetic structure is illustrated in Figure 4e,f, which is similar to that of $Li_2Mn(SO_4)_2$, which also orders in the same magnetic space group, albeit with an additional component along the *c*-axis.[17] The different magnetic moment orientation can likely arise from the different balance between spin exchange and spin−orbit coupling for d^5 Mn^{2+} and d^8 Ni^{2+}. Similar to marinite $Li_xM(SO_4)_2$ (M = Fe^{III}, Co^{II}, and Mn^{II}), the ground-state magnetic structure of marinite $Li_2Ni(SO_4)_2$ can be described by a propagation vector k = (0, 0, 0) and an alternating spin sequence (±) along the [011] direction. Essentially, the structure is built up of ferromagnetic layers arranged antiferromagnetically along the *b*-axis, following an A-type AFM spin ordering.

Optical Properties. The band gap of the novel *m*-$Li_2Ni(SO_4)_2$ phase was found from UV−visible−NIR spectroscopy. As shown in Figure 5a, the UV−visible absorption spectra were found to be comparable for both the *m*- and *o*-

https://doi.org/10.1021/acs.chemmater.1c01669
Chem. Mater. 2021, 33, 6108−6119

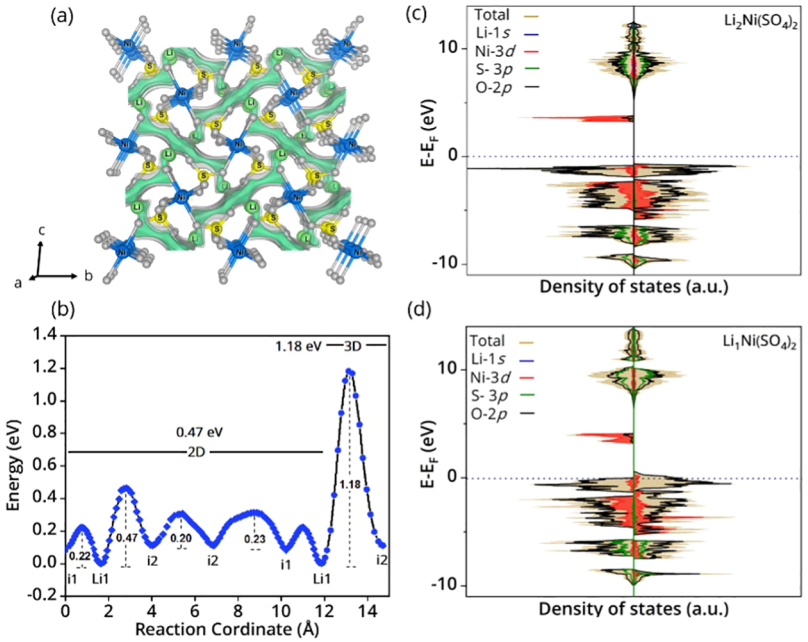

Figure 6. (a) Bond valence site energy (BVSE)-generated Li^+ ion migration pathways for *m*-$Li_2Ni(SO_4)_2$ shown using a ball-and-stick model. (b) Corresponding energy plot depicts the activation energy barrier for Li^+-ion migration. DFT calculations generated the total density of states and pDOS of the constituent elements of (c) pristine *m*-$Li_2Ni(SO_4)_2$ and (d) delithiated $LiNi(SO_4)_2$.

polymorphs of $Li_2Ni(SO_4)_2$, suggesting similar physical appearance (color) and electronic and optical band gaps. Various peaks in the spectra were assigned to the respective electronic d−d transition using Tanabe−Sugano diagrams.[42] Two peaks, observed in the visible region (1.55−3.10 eV), are linked to the $^3A_2$ to $^3T_1$ transition responsible for the ivory white color of the pristine powder samples.[43] Then, the optical band gap was obtained from the KM plot based on the simplified Kubelka−Munk (KM) theory (Figure 5b). The estimated optical band gaps of *m*-$Li_2Ni(SO_4)_2$ and *o*-$Li_2Ni(SO_4)_2$ were found to be 5.9 and 6 eV, respectively. These large values of the optical band gap are in agreement with the values reported for other cathode active materials such as $LiFePO_4$ and Li_2FeSiO_4,[44] implying the electronically insulating nature of $Li_2Ni(SO_4)_2$. This necessitates electrode optimization measures involving material optimization and intimate conductive carbon coating to enhance electronic conductivity to facilitate improved e-transfer coupled with the Li-ion (de)insertion process.

Li^+ Migration and Redox Activity in *m*-$Li_2Ni(SO_4)_2$. High Li^+ ion diffusivity and a low migration barrier are two primary features of efficient Li-ion battery insertion materials. The Li^+ migration barrier of the target material was calculated using a computationally economic bond valence site energy (BVSE) tool. The resulting isoenergy map illustrating Li^+ ion migration pathways for *m*-$Li_2Ni(SO_4)_2$ is shown in Figure 6a. It offers channels for Li^+ ion migration along the [100] direction across a zigzag path between two equivalent positions, forming 2D pathways accessible at an activation energy barrier of 0.47 eV (Figure 6b). It is noted that for *m*-$Li_2Fe(SO_4)_2$, there is a significant difference in the activation energy to access 1D and 2D channels. This difference decreases for *m*-$Li_2Co(SO_4)_2$ and, finally, there is only a 2D pathway for Li-ion migration in *m*-$Li_2Ni(SO_4)_2$. It is speculated that as the unit cell volume decreases while going from Fe to Ni transition metal, 1D pathways may start interacting with each other resulting in predominant 2D pathways for ionic migration. At higher charge voltage and within the electrolyte stability window, 3D migration pathways can be accessible with a migration barrier of 1.18 eV, which is slightly higher than 1.04 eV reported for isostructural *m*-$Li_2Fe(SO_4)_2$.[43] In contrast, the *o*-$Li_2Ni(SO_4)_2$ polymorph has distorted 3D migration pathways with an energy barrier of 0.67 eV (Figure S7). BVSE analysis confirms that both *m* and *o*-polymorphs of $Li_2Ni(SO_4)_2$ are suitable Li^+ conductors with potential application as cathode materials for Li-ion batteries.

In the bisulfate family, the $Li_2Fe(SO_4)_2$ polymorphs registered an average Fe^{2+}/Fe^{3+} redox potential at 3.83 V (vs Li^+/Li^0) with 1 M $LiClO_4$ dissolved in PC as the electrolyte solution.[14,15] Isostructural Mn- and Co-analogues exhibited the corresponding redox potentials at 4.54 and 5.2 V, respectively, in an especially concocted high-voltage sebaconitrile-based electrolyte.[45] This trend suggests the occurrence of Ni^{2+}/Ni^{3+} redox potential in the $Li_2Ni(SO_4)_2$ framework over 5.2 V. Despite various cathode optimizations, all efforts to activate the Ni^{2+}/Ni^{3+} redox activity in *m*-$Li_2Ni(SO_4)_2$, using conventional organic electrolytes (such as 1 M $LiClO_4$/PC or 1 M $LiPF_6$/EC-PC−DMC), were unfruitful. As the existing electrolytes are unstable above 4.8 V, the development of high-voltage electrolytes can help in triggering redox activity in *m*-$Li_2Ni(SO_4)_2$. At this juncture, to gauge the potential Ni^{2+}/Ni^{3+} redox couple in novel *m*-$Li_2Ni(SO_4)_2$, first-principles density functional theory (DFT) calculations were performed to acquire information about the electronic band structure.

The experimental and DFT calculation-predicted (based on GGA + *U* approximation) values of the lattice parameters are listed in Table 2. With less than 7% difference in the lattice parameters between the experimentally synthesized compound and the chosen model, the selected model was found suitable for further calculation. Further, we predict ∼13% change in volume ($\Delta V/V$) on Li removal from $Li_2Ni(SO_4)_2$ in sync with an earlier experimental report on $Li_2Fe(SO_4)_2$.[43] The projected

https://doi.org/10.1021/acs.chemmater.1c01669
Chem. Mater. 2021, 33, 6108−6119

Table 2. Optimized Lattice Parameters of *m*-$Li_2Ni(SO_4)_2$ Estimated Using GGA + *U* Approximation, Compared with Experimental Values[a]

parameter	experimental	*m*-$Li_2Ni(SO_4)_2$ [GGA + *U*]	$Li_1Ni(SO_4)_2$ [GGA + *U*]
a (Å)	4.9646(2)	4.89939	5.07746
b (Å)	8.0166(3)	7.76163	6.15325
c (Å)	8.7312(4)	8.53119	9.17404
β (°)	121.8804(10)	121.7958	123.5612
V (Å^3)	295.08(2)	275.7325	238.8422

[a]Crystal structure having $P2_1/c$ symmetry was chosen as a reference model.

density of states (pDOS) of the constituent elements and the total density of state (DOS) of *m*-$Li_2Ni(SO_4)_2$ are shown in Figure 6c. The parent compound, fully lithiated $Li_2Ni(SO_4)_2$, has an electronic band gap of 3.83 eV. Further, a trapped state is observed near the Fermi level in the energy range of 0.5−5 eV with the main contribution from the Ni 3d orbital, which may result in polaronic conductivity as reported for $LiFePO_4$ and $Li_2Fe(SO_4)_2$.[43,44] At the valence band edge, we observe a major contribution from O 2p and Ni 3d orbitals, suggesting inclination of the O 2p orbital to be involved in the redox reaction with a minor contribution from the Ni 3d orbital. The increased S 3p orbital contribution is evident in the deeper energy level of DOS, confirming stronger covalent bonding between sulfur and oxygen atoms. The DOS of the $LiNi(SO_4)_2$ (delithiated) compound is illustrated in Figure 6d. Here, the Fermi level crosses the down spin states with increased contribution of the O 2p orbital in comparison to the Ni 3d orbital, suggesting a transition from semiconductor to semimetallic behavior on delithiation. The strong contribution of the O 2p orbital near the Fermi state in the pDOS of delithiated $LiNi(SO_4)_2$ implies the complete delithiation reaction to $Ni(SO_4)_2$ to be centered on the O atom (anionic redox). It is also noted that delithiation does not affect the S−O bonding nature as S 3p and O 2p orbital hybridization remains the same, as also evident from the constant average S−O bond length (Tables S6 and S7). The minor involvement of the Ni redox activity during delithiation is hinted at from the variation of the average atomic magnetic moment of Ni and O atoms. The average magnetic moment of Ni varies from 1.781 μ_B to 1.616 μ_B (Δ = 9%), while O atom experiences a dramatic change from 0.02 μ_B to 0.07 μ_B (Δ = 250%). A detailed investigation probing the mechanism of anionic redox activity in bisulfate $Li_2M(SO_4)_2$ polyanionic systems is under progress.

Cell voltage is a key parameter dictating the energy density of batteries. Using first-principles calculations, the energy of the intermediate compound was estimated during the delithiation process. The average cell voltage can be predicted by the following equation

$$V = \frac{-|E(Li_2Ni(SO_4)_2 - E(Li_{2-x}Ni(SO_4)_2 - xE(Li)|}{x \cdot e}$$

where *E* and *x* are the energy and the number of lithium atoms involved in the redox reaction, respectively. Inspecting various configurations of lithium sites and vacancies related to half (x = 1) and full delithiation (x = 0), the most stable configuration and the corresponding energy were used for further calculations. The average deintercalation potential (anionic redox) is predicted to be 5.5 V during Li concentration variation in the range $2 < x < 1$ per unit formula, in sync with Ni-based compounds like Li_2NiPO_4F having 5.3 V activity upon Li (de)insertion.[46] Such a high Ni^{2+}/Ni^{3+} redox potential can only be tested in the presence of electrolyte having an electrochemical stability window beyond 6 V. With the future development of electrolytes, the $Li_2Ni(SO_4)_2$ compound can potentially work as a high-voltage cathode material for Li-ion batteries.

DISCUSSION

Except for oxysulfate $Fe_2O(SO_4)_2$, polyanionic sulfate (SO_4^{2-}) cathode materials are inherently prone to moisture attack as reported for (Li)$FeSO_4OH$, $LiFeSO_4F$, and $Li_2Fe(SO_4)_2$ polymorphs. This is due to the comparable Lewis basicity of oxygen atom in both SO_4^{2-} (~0.17 v.u.) and H_2O (~0.25 v.u.) groups.[47] The moisture sensitivity of both polymorphs of $Li_2Ni(SO_4)_2$ was tested by exposing the as-prepared materials to ambient atmosphere (open air) for 2 weeks. Postmortem XRD patterns showed a significant difference (Figure S8). Degradation of pristine *m*-$Li_2Ni(SO_4)_2$ was observed with the complete disappearance of the first characteristic (011) reflection peak (at 16.31°) and the appearance of new peaks resulting from the formation of hydrated precursor phases, viz., $NiSO_4 \cdot 6H_2O$ ($P4_12_12$#92) and $Li_2SO_4 \cdot H_2O$ ($P2_1$#5). Similar moisture-induced material degradation was noticed for the *o*-$Li_2Ni(SO_4)_2$ phase. Using semiquantitative analysis based on the reference intensity ratio technique,[48] both *m*- and *o*-polymorphs were quantified to degrade to a precursor ratio of 64:36 and 69:31 ($NiSO_4 \cdot 6H_2O/Li_2SO_4 \cdot H_2O$), respectively. Then, infrared (FTIR) analysis was conducted on both polymorphs. The absorption spectra of pristine and air-exposed powders acquired in ATR mode are compared in Figure 7. Pristine bisulfates have no trace of water evident from

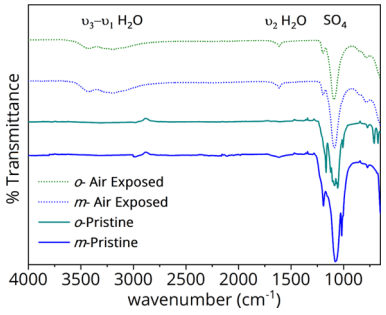

Figure 7. FTIR spectra, acquired in ATR mode, of *m*-$Li_2Ni(SO_4)_2$ and *o*-$Li_2Ni(SO_4)_2$ phases before and after air exposure.

the absence of any band in the vicinity of 3500 and 1595 cm^{-1} assigned to three fundamental molecular vibrations in (a)symmetric stretching and bending of OH^- species, respectively. In the low-wavenumber window, signature SO_4 bands were observed attributed to symmetric stretching (~980 cm^{-1}), asymmetric stretching (~1100 cm^{-1}), and asymmetric bending (~610 cm^{-1}).[49] The two polymorphs exhibit different FTIR spectra consistent with the presence of two crystallographically distinct sulfate SO_4 tetrahedra in the *o*-phase compared to only one type in the *m*-phase. For the new monoclinic $Li_2Ni(SO_4)_2$, band splitting is absent near 1160 cm^{-1}, indicating higher sulfate bonding symmetry as compared to the $Li_2M(SO_4)_2$ (M = Mn, Fe, Co) analogues having C_{3v} bonding symmetry. The sulfate bonding symmetry in *o*-polymorph is C_1 in agreement with the literature.[16] On exposure to ambient atmosphere, the FTIR spectra were

https://doi.org/10.1021/acs.chemmater.1c01669
Chem. Mater. 2021, 33, 6108−6119

observed to change remarkably, with intense absorption bands in regions assigned to water molecule (~3200−3500 cm^{-1}). Further, in both cases, the characteristic bands in the lower-wavenumber region are notably alike, corroborating formation of similar hydrated precursor phases as established above. Thus, bisulfate cathode materials should be carefully stored and handled in an inert ambience.

The successful synthesis of novel marinite *m*-$Li_2Ni(SO_4)_2$ using the spray drying route extends polymorphism to the $Li_2Ni(SO_4)_2$ compound, a member of the bisulfate $Li_2M(SO_4)$ (M = Mn, Fe, Co, Ni) family. The finding builds on an earlier report[15] showing inclination of metallic bisulfate compounds having a smaller transition metal cation [$r(Ni^{2+})$ = 0.69 Å] to stabilize in the *o*-phase, whereas compounds having a larger transition metal cation [$r(Mn^{2+})$ = 0.83 Å] stabilize in the *m*-phase.[50] Observing the volume per formula unit (V/Z) vs ionic radii (M^{2+}) plot (Figure 8a), it is noted that V/Z of novel *m*-

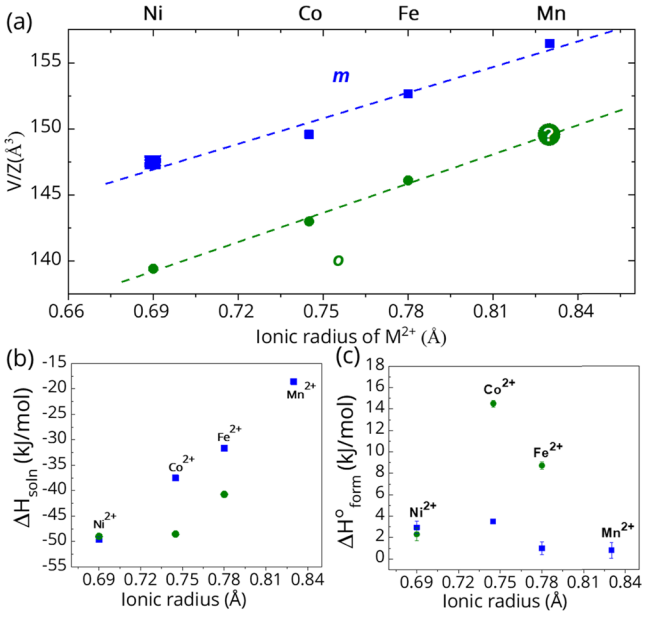

Figure 8. (a) Volume per formula unit (V/Z) plotted as a function of ionic radii of M^{2+} in the $Li_2M(SO_4)_2$ (M = Mn, Fe, Co, and Ni) family. The dashed blue (monoclinic) and green (orthorhombic) lines are linearly fitted lines. Novel *m*-$Li_2Ni(SO_4)_2$ follows a linear trend as a function of ionic radius (shown by a large blue square). The possible volume of the yet unknown *o*-$Li_2Mn(SO_4)_2$ is indicated by the question mark. Enthalpies of (b) dissolution in 5 M HCl at 25 °C and (c) formation from Li_2SO_4 and MSO_4 at 25 °C of $Li_2M(SO_4)_2$ (M = Mn, Fe, Co, and Ni) compounds. Blue and green represent the monoclinic and orthorhombic polymorphs of $Li_2M(SO_4)_2$, respectively. Except for *m*-$Li_2Ni(SO_4)_2$, the remaining V/Z, ΔH_{soln}, and ΔH°_{form} values have been taken from the literature to arrive at an overall picture.[14−17] The unit cell volume for each sample is derived from the Rietveld analysis of the NPD data.

$Li_2Ni(SO_4)_2$ (V = 295.08(2) $Å^3$ and Z = 2) follows a linear trend obtained after linearly fitting (R^2 = 0.97) the respective values of *m*-$Li_2M(SO_4)_2$ (M = Mn, Fe, Co, and Ni). A similar linear trend (R^2 = 0.99) was also noted for available orthorhombic counterparts. On extrapolation, the unit cell volume of unknown *o*-$Li_2Mn(SO_4)_2$ is expected to be ~1196.8 $Å^3$ (with V/Z = 149.6 $Å^3$). Based on a previous report,[43] the hypothetical *o*-$Li_2Mn(SO_4)_2$ phase may crystallize at higher pressure beyond 13 GPa. This idea is not far-fetched as *m*-$Li_2Co(SO_4)_2$ exhibits pressure-induced phase transformation to *o*-$Li_2Co(SO_4)_2$ beyond 3.65 GPa. The synthesis of *o*-$Li_2Mn(SO_4)_2$ remains a task for solid-state chemists to complete the bisulfate family of polymorphs.

Essentially, the following question remains: what are the factors responsible for crystallization of *m*-$Li_2Ni(SO_4)_2$ using the spray drying route while the conventional ceramic and high-energy ball-milling route failed? To this end, the enthalpy of formation of *m*-$Li_2Ni(SO_4)_2$ was determined using isothermal acid solution calorimetry (Tables 3 and 4). The

Table 3. Calorimetric Data for *m*-$Li_2Ni(SO_4)_2$ and *o*-$Li_2Ni(SO_4)_2$ Formation[a]

composition	ΔH_{solun} (kJ/mol)	ΔH°_{form} (kJ/mol)
Li_2SO_4	3.42 ± 0.06 (4)	
$NiSO_4$	−50.08 ± 0.05 (5)	
m-$Li_2Ni(SO_4)_2$	−49.61 ± 0.56 (7)	2.95 ± 0.57
o-$Li_2Ni(SO_4)_2$	−49.00 ± 0.30 (8)	2.34 ± 0.58

[a]Errors are two standard deviations of the mean. Values in parentheses are the number of measurements. Enthalpies of formation are from the binary sulfates and are the same within the uncertainties.

enthalpy of dissolution for *m*-$Li_2Ni(SO_4)_2$ is −49.61 ± 0.56 kJ/mol and *o*-$Li_2Ni(SO_4)_2$ is −49.00 ± 0.30 kJ/mol; the values are essentially the same within the experimental error. Finally, the enthalpies of formation of $Li_2Ni(SO_4)_2$ from its constituent binary sulfates, Li_2SO_4 and $NiSO_4$, were calculated using the thermochemical cycle, as shown in Table 4. Figure 8b,c shows the relative energetic stabilities of the monoclinic and orthorhombic phases of $Li_2M(SO_4)_2$ (M = Mn, Fe, Co, Ni) in terms of dissolution and formation enthalpies as a function of ionic radius. It does appear that the orthorhombic form may be energetically slightly more stable than the monoclinic analogue, which is supported by DSC data (Figure S2). The data follow the general trend that the dissolution enthalpy becomes more exothermic with a decrease in the cation size as reported in a previous study.[16] The enthalpies of formation for both *m*- and *o*-$Li_2Ni(SO_4)_2$ from binary sulfates are slightly positive. The lower-symmetry monoclinic polymorph is energetically slightly less stable than the higher-symmetry orthorhombic polymorph. Driven by thermodynamic metastability, *m*-$Li_2Ni(SO_4)_2$ transforms irreversibly into *o*-$Li_2Ni(SO_4)_2$ on (i) heat treatment (Figure 3) and (ii) longer annealing time at formation temperature (Figure S9), clearly illustrating the role of both thermodynamic and kinetic factors in phase stability. The thermal-phase stability is in contrast to that observed in $Li_2M(SO_4)_2$ (M = Co, Fe), where the orthorhombic phase transforms into the monoclinic phase on heating.[16] Overall, in this bisulfate $Li_2M(SO_4)_2$ (M = Mn, Co, Fe, Ni) family, while larger cations [e.g., $Li_2Mn(SO_4)_2$] form a stable monoclinic phase, smaller cations [ca. $Li_2Ni(SO_4)_2$] tend to form a stable orthorhombic phase.

The transition enthalpy (ΔH_{tr}) at 25 °C was determined from the enthalpy of dissolution of monoclinic and orthorhombic $Li_2M(SO_4)_2$ using the cycle; ΔH_{tr} ($o \rightarrow m$) for $Li_2Fe(SO_4)_2$ and $Li_2Co(SO_4)_2$ is −7.74 ± 0.60 and −11.00 ± 0.34 kJ/mol, respectively, whereas from *m*-$Li_2Ni(SO_4)_2 \rightarrow$ *o*-$Li_2Ni(SO_4)_2$, it is −0.61 ± 0.5 kJ/mol (Table 5). The transition enthalpy being exothermic indicates that *m*-$Li_2Fe(SO_4)_2$, *m*-$Li_2Co(SO_4)_2$, and *o*-$Li_2Ni(SO_4)_2$ are the energetically stable phases, though the role of entropy is not known. The energy difference between *m*-$Li_2Ni(SO_4)_2$ and *o*-Li_2Ni-

https://doi.org/10.1021/acs.chemmater.1c01669
Chem. Mater. 2021, 33, 6108−6119

Table 4. Thermochemical Cycles for Enthalpy of Formation for *m*-$Li_2Ni(SO_4)_2$

	enthalpy measurement
$Li_2Ni(SO_4)_{2(s,\ 25\ °C)} + 4HCl_{(l,\ 25\ °C)} \rightarrow 2LiCl_{(sln,\ 25\ °C)} + NiCl_{2(sln,\ 25\ °C)} + 2H_2SO_{4(sln,\ 25\ °C)}$	$\Delta H_1 = \Delta H_{solun}\ (Li_2Ni(SO_4)_2)$
$Li_2SO_{4(s,\ 25\ °C)} + 2HCl_{(l,\ 25\ °C)} \rightarrow 2LiCl_{(sln,\ 25\ °C)} + H_2SO_{4(sln,\ 25\ °C)}$	$\Delta H_2 = \Delta H_{solun}\ (Li_2SO_4)$
$NiSO_{4(s,\ 25\ °C)} + 2HCl_{(l,\ 25\ °C)} \rightarrow NiCl_{2(sln,\ 25\ °C)} + H_2SO_{4(sln,\ 25\ °C)}$	$\Delta H_3 = \Delta H_{solun}\ (NiSO_4)$
$Li_2SO_{4(s,\ 25\ °C)} + NiSO_{4(s,\ 25\ °C)} \rightarrow Li_2Ni(SO_4)_{2(s,\ 25\ °C)}$	$\Delta H_4 = \Delta H^{\circ}_{form}\ (Li_2Ni(SO_4)_2) = -\Delta H_1 + \Delta H_2 + \Delta H_3$

Table 5. Thermochemical Cycle for the Determination of the Transition Enthalpy at 25 °C in $Li_2M(SO_4)_2$ (M = Fe, Co, Ni)

reaction	ΔH (kJ/mol)
$o\text{-}Li_2Fe(SO_4)_{2(s,\ 25\ °C)} \rightarrow Li_2SO_{4(sln,\ 25\ °C)} + FeSO_{4(sln,\ 25\ °C)}$	$\Delta H_5 = -40.75 \pm 0.40$
$m\text{-}Li_2Ni(SO_4)_{2(s,\ 25\ °C)} \rightarrow Li_2SO_{4(sln,\ 25\ °C)} + FeSO_{4(sln,\ 25\ °C)}$	$\Delta H_6 = -33.01 \pm 0.45$
$o\text{-}Li_2Co(SO_4)_{2(s,\ 25\ °C)} \rightarrow Li_2SO_{4(sln,\ 25\ °C)} + CoSO_{4(sln,\ 25\ °C)}$	$\Delta H_7 = -48.54 \pm 0.28$
$m\text{-}Li_2Ni(SO_4)_{2(s,\ 25\ °C)} \rightarrow Li_2SO_{4(sln,\ 25\ °C)} + CoSO_{4(sln,\ 25\ °C)}$	$\Delta H_8 = -37.54 \pm 0.20$
$o\text{-}Li_2Ni(SO_4)_{2(s,\ 25\ °C)} \rightarrow Li_2SO_{4(sln,\ 25\ °C)} + NiSO_{4(sln,\ 25\ °C)}$	$\Delta H_9 = -40.75 \pm 0.40$
$m\text{-}Li_2Ni(SO_4)_{2(s,\ 25\ °C)} \rightarrow Li_2SO_{4(sln,\ 25\ °C)} + NiSO_{4(sln,\ 25\ °C)}$	$\Delta H_1 = -49.00 \pm 0.30$
$o\text{-}Li_2Fe(SO_4)_{2(s,\ 25\ °C)} \rightarrow m\text{-}Li_2Ni(SO_4)_{2(s,\ 25\ °C)}$	$\Delta H_{10} = \Delta H_5 - \Delta H_6$
$o\text{-}Li_2Co(SO_4)_{2(s,\ 25\ °C)} \rightarrow m\text{-}Li_2Ni(SO_4)_{2(s,\ 25\ °C)}$	$\Delta H_{11} = \Delta H_7 - \Delta H_8$
$m\text{-}Li_2Ni(SO_4)_{2(s,\ 25\ °C)} \rightarrow o\text{-}Li_2Ni(SO_4)_{2(s,\ 25\ °C)}$	$\Delta H_{12} = \Delta H_1 - \Delta H_9$

$(SO_4)_2$ is small compared to the values for $Li_2Fe(SO_4)_2$ and $Li_2Co(SO_4)_2$ analogues.

Synthesis routes are known to dictate the product phase assembly. In this bisulfate family, thermodynamically stable phases are formed by high-temperature ceramic routes and metastable phases are formed by ball-milling at room temperatures. Generally, the soft chemical approach is reported to favor formation of the metastable phase such as Tavorite $LiFeSO_4OH$, whereas its stable layered polymorph is stabilized using the conventional solid-state route and ball-milling route.[51] Further, the dehydration rate of the precursor plays a critical role in controlling the phase stability between the tavorite and triplite phases in $LiFe_{1-x}Mn_xSO_4F$ solid solution, where the slow rate of dehydration favors the tavorite phase over the triplite phase and vice versa.[52] Overall, an earlier report demonstrates that the entropy term plays a key role in the synthesis, stability, and phase formation among the polymorphs of Li-polyanionic compounds. As a trend, the synthesis requires induction of large disorder in the system, generating defects by ball-milling at room temperature[16,48] or arresting the initially formed metastable phase by spray drying. In the same line, the spray drying synthesis route, employed in the present work involving quick drying of intimately mixed aqueous precursor slurry, is speculated to arrest the intermediate phase near metastable *m*-$Li_2Ni(SO_4)_2$ at low temperatures, which irreversibly transforms into stable *o*-$Li_2Ni(SO_4)_2$ at higher temperatures.

CONCLUSIONS

A novel monoclinic $Li_2Ni(SO_4)_2$ bisulfate cathode for Li-ion batteries has been discovered and synthesized using the scalable aqueous spray drying route, extending polymorphism to Ni-analogue of the metallic bisulfate family. Apart from arresting the intermediate phase responsible for nucleation of the *m*-$Li_2Ni(SO_4)_2$ phase, spray drying forms a scalable economic route yielding nanoparticles with a porous spherical morphology suitable for battery application. *m*-$Li_2Ni(SO_4)_2$ assumes a monoclinic three-dimensional framework (s.g. $P2_1/c$) built from corner-sharing NiO_6 and SO_4 polyhedra. It renders long-range antiferromagnetic (AFM) ordering below 15 K. This marinite mineral class of $Li_2Ni(SO_4)_2$ is moderately moisture-sensitive and electronically insulating with a large optical band gap. As per BVSE and *ab initio* DFT calculations, this novel compound offers two-dimensional Li^+ migration pathways and can work as a high-voltage (ca. 5.5 V vs Li^+/Li^0) cathode involving both cationic ($Ni^{II/III}$) and anionic (O^-) redox activity with the possibility of polaronic conductivity. With the advent of stable high-voltage electrolytes, *m*-$Li_2Ni(SO_4)_2$ can be useful as a high-voltage cathode material for Li-ion batteries. This discovery underscores the role of soft chemistry routes such as spray drying in unveiling new insertion materials. It further demonstrates the richness of structural chemistry and polymorphism in SO_4-based polyanionic battery cathode materials.

ASSOCIATED CONTENT

Supporting Information

The Supporting Information is available free of charge at https://pubs.acs.org/doi/10.1021/acs.chemmater.1c01669.

Crystallographic data (CIF)

Crystallographic details of *m*-$Li_2Ni(SO_4)_2$ and *o*-$Li_2Ni(SO_4)_2$ using laboratory-scale; synchrotron and neutron diffraction; thermal analysis (TG-DSC); structural illustration and BVSE migration pathways for *o*-$Li_2Ni(SO_4)_2$; bond length, Baur's distortion, and bond angle variance for *m*-$Li_2Ni(SO_4)_2$ and *o*-$Li_2Ni(SO_4)_2$ polymorphs; XRD patterns of moisture-infected bisulfates; and structural parameters generated from DFT calculations (PDF)

AUTHOR INFORMATION

Corresponding Author

Prabeer Barpanda − *Faraday Materials Laboratory (FaMaL), Materials Research Centre, Indian Institute of Science, Bangalore 560012, India;* orcid.org/0000-0003-0902-3690; Email: prabeer@iisc.ac.in; Fax: +91 80 2360 7316; www.prabeer.org

Authors

Shashwat Singh − *Faraday Materials Laboratory (FaMaL), Materials Research Centre, Indian Institute of Science, Bangalore 560012, India*

https://doi.org/10.1021/acs.chemmater.1c01669
Chem. Mater. 2021, 33, 6108−6119

Pawan Kumar Jha − *Faraday Materials Laboratory (FaMaL), Materials Research Centre, Indian Institute of Science, Bangalore 560012, India*
Maxim Avdeev − *Australian Nuclear Science and Technology Organisation, Lucas Heights, NSW 2234, Australia; School of Chemistry, The University of Sydney, Sydney 2006, Australia;* orcid.org/0000-0003-2366-5809
Wenli Zhang − *Materials Science and Engineering, King Abdullah University of Science and Technology (KAUST), Thuwal 23955-6900, Saudi Arabia*
K. Jayanthi − *School of Molecular Sciences and Center for Materials of the Universe, Arizona State University, Tempe, Arizona 85287, United States;* orcid.org/0000-0002-5016-3575
Alexandra Navrotsky − *School of Molecular Sciences and Center for Materials of the Universe, Arizona State University, Tempe, Arizona 85287, United States;* orcid.org/0000-0002-3260-0364
Husam N. Alshareef − *Materials Science and Engineering, King Abdullah University of Science and Technology (KAUST), Thuwal 23955-6900, Saudi Arabia;* orcid.org/0000-0001-5029-2142

Complete contact information is available at: https://pubs.acs.org/10.1021/acs.chemmater.1c01669

Notes

The authors declare no competing financial interest.

■ ACKNOWLEDGMENTS

The authors acknowledge the financial support from the Technology Mission Division (Department of Science and Technology, Government of India) under the Materials for Energy Storage (MES-2018) program (DST/TMD/MES/2K18/207). S.S. and P.K.J. thank the Ministry of Human Resource Development (MHRD) for financial support. P.K.J. thanks Prof. M. Shrivastava and Prof. S. G. Gopalakrishnan for computational resources and scientific discussions, respectively. H.N.A. is grateful to the King Abdullah University of Science and Technology (KAUST) for partial financial support. A.N. and K.J. sincerely acknowledge financial support from the U.S. Department of Energy, Office of Basic Energy Sciences, Grant DE-FG02-03ER46053.

■ REFERENCES

(1) Manthiram, A.; Goodenough, J. B. Lithium insertion into $Fe_2(SO_4)_3$ frameworks. *J. Power Sources* **1989**, *26*, 403−408.
(2) Padhi, A. K.; Nanjundaswamy, K. S.; Masquelier, C.; Okada, S.; Goodenough, J. B. Effect of structure on the Fe^{3+}/Fe^{2+} redox couple in iron phosphates. *J. Electrochem. Soc.* **1997**, *144*, 1609−1613.
(3) Padhi, A. K.; Nanjundaswamy, K. S.; Goodenough, J. B. Phospho-olivines as positive-electrode materials for rechargeable lithium batteries. *J. Electrochem. Soc.* **1997**, *144*, 1188−1194.
(4) Barpanda, P.; Dwibedi, D.; Ghosh, S.; Kee, Y.; Okada, S. Lithium metal borate ($LiMBO_3$) family of insertion materials for Li-ion batteries: A sneak peak. *Ionics* **2015**, *21*, 1801−1812.
(5) Barpanda, P.; Nishimura, S.; Yamada, A. High-voltage pyrophosphate cathodes. *Adv. Energy Mater.* **2012**, *2*, 841−859.
(6) Sharma, L.; Adiga, S. P.; Alshareef, H. N.; Barpanda, P. Fluorophosphates: Next generation cathode materials for rechargeable batteries. *Adv. Energy Mater.* **2020**, *10*, No. 2001449.
(7) Islam, M. S.; Dominko, R.; Masquelier, C.; Sirisopanaporn, C.; Armstrong, A. R.; Bruce, P. G. Silicate cathodes for lithium batteries: alternatives to phosphates? *J. Mater. Chem.* **2011**, *21*, 9811−9818.
(8) Barpanda, P. Pursuit of Sustainable Iron-Based Sodium Battery Cathodes: Two Case Studies. *Chem. Mater.* **2016**, *28*, 1006−1011.
(9) Recham, N.; Chotard, J. N.; Dupont, L.; Delacourt, C.; Walker, W.; Armand, M.; Tarascon, J. M. A 3.6 V lithium-based fluorosulphate insertion positive electrode for lithium-ion batteries. *Nat. Mater.* **2010**, *9*, 68−74.
(10) Barpanda, P.; Ati, M.; Melot, B. C.; Rousse, G.; Chotard, J. N.; Doublet, M. L.; Sougrati, M. T.; Corr, S. A.; Jumas, J. C.; Tarascon, J. M. A 3.90 V iron-based fluorosulphate material for lithium-ion batteries crystallizing in the triplite structure. *Nat. Mater.* **2011**, *10*, 772−779.
(11) Barpanda, P. Sulphate chemistry for high-voltage insertion materials: Synthetic, structural and electrochemical insights. *Isr. J. Chem.* **2015**, *55*, 537−557.
(12) Barpanda, P.; Oyama, G.; Nishimura, S.; Chung, S. C.; Yamada, A. A 3.8 V earth-abundant sodium battery electrode. *Nat. Commun.* **2014**, *5*, No. 4358.
(13) Recham, N.; Rousse, G.; Sougrati, M. T.; Chotard, J.-N.; Frayret, C.; Mariyappan, S.; Melot, B. C.; Jumas, J.-C.; Tarascon, J. M. Preparation and characterization of a stable $FeSO_4F$-based framework for alkali ion insertion electrodes. *Chem. Mater.* **2012**, *24*, 4363−4370.
(14) Reynaud, M.; Ati, M.; Melot, B. C.; Sougrati, M. T.; Rousse, G.; Chotard, J.-N.; Tarascon, J.-M. $Li_2Fe(SO_4)_2$ as a 3.83 V positive electrode material. *Electrochem. Commun.* **2012**, *21*, 77−80.
(15) Lander, L.; Reynaud, M.; Rousse, G.; Sougrati, M. T.; Laberty-Robert, C.; Messinger, R. J.; Deschamps, M.; Tarascon, J.-M. Synthesis and electrochemical performance of the orthorhombic $Li_2Fe(SO_4)_2$ polymorph for Li-ion batteries. *Chem. Mater.* **2014**, *26*, 4178−4189.
(16) Radha, A. V.; Lander, L.; Rousse, G.; Tarascon, J. M.; Navrotsky, A. Thermodynamic stability and correlation with synthesis conditions, structure and phase transformations in orthorhombic and monoclinic $Li_2M(SO_4)_2$ (M = Mn, Fe, Co, Ni) polymorphs. *J. Mater. Chem. A* **2015**, *3*, 2601−2608.
(17) Reynaud, M.; Rousse, G.; Chotard, J.-N.; Rodríguez-Carvajal, J.; Tarascon, J.-M. Marinite $Li_2M(SO_4)_2$ (M = Co, Fe, Mn) and $Li_1Fe(SO_4)_2$: Model compounds for super-super-exchange magnetic interactions. *Inorg. Chem.* **2013**, *52*, 10456−10466.
(18) Lander, L.; Reynaud, M.; Rodríguez-Carvajal, J.; Tarascon, J.-M.; Rousse, G. Magnetic structures of orthorhombic $Li_2M(SO_4)_2$ (M = Co, Fe) and $Li_xFe(SO_4)_2$ (x = 1, 1.5) phases. *Inorg. Chem.* **2016**, *55*, 11760−11769.
(19) Reynaud, M.; Rodríguez-Carvajal, J.; Chotard, J.-N.; Tarascon, J.-M.; Rousse, G. Magnetic structure and properties of orthorhombic $Li_2Ni(SO_4)_2$: A possible magnetoelectric material. *Phys. Rev. B* **2014**, *89*, No. 104419.
(20) Dwibedi, D.; Baskar, S.; Barpanda, P. Sustainable aqueous synthesis and electrochemical insights on high-voltage sodium alluaudite insertion materials. *ECS Trans.* **2017**, *80*, 337−342.
(21) Rahaman, M. N. *Ceramic Processing and Sintering*, 2nd ed.; CRC Press, 2003.
(22) Rietveld, H. A profile refinement method for nuclear and magnetic structures. *J. Appl. Crystallogr.* **1969**, *2*, 65−71.
(23) Larson, A.; Von Dreele, R. J. *Report LAUR 86-748*; Los Alamos National Laboratory: New Mexico, 2000.
(24) Toby, B. H. EXPGUI, a graphical user interface for GSAS. *J. Appl. Crystallogr.* **2001**, *34*, 210−213.
(25) Momma, K.; Izumi, F. VESTA 3 for three-dimensional visualization of crystal, volumetric and morphology data. *J. Appl. Crystallogr.* **2011**, *44*, 1272−1276.
(26) Avdeev, M.; Hester, J. R. ECHIDNA: a decade of high-resolution neutron powder diffraction at OPAL. *J. Appl. Crystallogr.* **2018**, *51*, 1597−1604.
(27) Hodges, L.; Lang, N. D.; Ehrenreich, H.; Freeman, A. J. Magnetic form factor of nickel. *J. Appl. Phys.* **1966**, *37*, 1449.
(28) Kubelka, P. New contributions to the optics of intensely light-scattering materials. Part I. *J. Opt. Soc. Am.* **1948**, *38*, 448−457.

(29) López, R.; Gómez, R. Band-gap energy estimation from diffuse reflectance measurements on sol−gel and commercial TiO_2: a comparative study. *J. Sol-Gel Sci. Technol.* **2012**, *61*, 1−7.
(30) Zones, S. I.; Jayanthi, K.; Pascual, J.; Xie, D.; Navrotsky, A. Energetics of the local environment of structure-directing agents influence zeolite synthesis. *Chem. Mater.* **2021**, *33*, 2126−2138.
(31) Kilday, M. V. The enthalpy of solution of SRM 1655 (KCl) in H_2O. *J. Res. Natl. Bur. Stand.* **1980**, *85*, 467−481.
(32) Brown, I. D. *The Chemical Bond in Inorganic Chemistry: The Bond Valence Model*; Oxford University Press, 2016; Vol. *27*.
(33) Adams, S.; Rao, R. P. Transport pathways for mobile ions in disordered solids from the analysis of energy-scaled bond-valence mismatch landscapes. *Phys. Chem. Chem. Phys.* **2009**, *11*, 3210−3216.
(34) Kresse, G.; Hafner, J. Ab initio molecular dynamics for liquid metals. *Phys. Rev. B* **1993**, *47*, 558−561.
(35) Kresse, G.; Furthmüller, J. Efficient iterative schemes for ab initio total-energy calculations using a plane-wave basis set. *Phys. Rev. B* **1996**, *54*, 11169−11186.
(36) Perdew, J. P.; Burke, K.; Ernzerhof, M. Generalized Gradient Approximation made simple. *Phys. Rev. Lett.* **1996**, *77*, 3865−3868.
(37) Dudarev, S. L.; Botton, G. A.; Savrasov, S. Y.; Humphreys, C. J.; Sutton, A. P. Electron-energy-loss spectra and the structural stability of nickel oxide: An LSDA+U study. *Phys. Rev. B* **1998**, *57*, 1505−1509.
(38) Framinan, J. M.; Leisten, R.; Ruiz García, R. A Case Study: Ceramic Tile Production. In *Manufacturing Scheduling Systems: An Integrated View on Models, Methods and Tools*; Springer: London, 2014; pp 371−395.
(39) Clark, J. M.; Eames, C.; Reynaud, M.; Rousse, G.; Chotard, J.-N.; Tarascon, J.-M.; Islam, M. S. High voltage sulphate cathodes $Li_2M(SO_4)_2$ (M = Fe, Mn, Co): atomic-scale studies of lithium diffusion, surfaces and voltage trends. *J. Mater. Chem. A* **2014**, *2*, 7446−7453.
(40) Dwibedi, D.; Gond, R.; Dayamani, A.; Araujo, R. B.; Chakraborty, S.; Ahuja, R.; Barpanda, P. $Na_{2.32}Co_{1.84}(SO_4)_3$ as a new member of the alluaudite family of high-voltage sodium battery cathodes. *Dalton Trans.* **2017**, *46*, 55−63.
(41) Stokes, H. T.; Hatch, D. M.; Campbell, B. J. ISOTROPY Software Suite. http://iso.byu.edu.
(42) Tanabe, Y.; Sugano, S. On the absorption spectra of complex ions II. *J. Phys. Soc. Jpn.* **1954**, *9*, 766−779.
(43) Lander, L.; Reynaud, M.; Carrasco, J.; Katcho, N. A.; Bellin, C.; Polian, A.; Baptiste, B.; Rousse, G.; Tarascon, J.-M. Unveiling the electrochemical mechanisms of $Li_2Fe(SO_4)_2$ polymorphs by neutron diffraction and density functional theory calculations. *Phys. Chem. Chem. Phys.* **2016**, *18*, 14509−14519.
(44) Zhou, F.; Kang, K.; Maxisch, T.; Ceder, G.; Morgan, D. The electronic structure and band gap of $LiFePO_4$ and $LiMnPO_4$. *Solid State Commun.* **2004**, *132*, 181−186.
(45) Muthiah, A.; Baikie, T.; Ulaganathan, M.; Copley, M.; Yang, G.; Aravindan, V.; Srinivasan, M. Structural, thermal, and electrochemical studies of novel $Li_2Co_xMn_{1-x}(SO_4)_2$ bimetallic sulfates. *J. Phys. Chem. C* **2017**, *121*, 24971−24978.
(46) Nagahama, M.; Hasegawa, N.; Okada, S. High voltage performances of Li_2NiPO_4F cathode with dinitrile-based electrolytes. *J. Electrochem. Soc.* **2010**, *157*, A748−A752.
(47) Zhang, L.; Tarascon, J.-M.; Sougrati, M. T.; Rousse, G.; Chen, G. Influence of relative humidity on the structure and electrochemical performance of sustainable $LiFeSO_4F$ electrodes for Li-ion batteries. *J. Mater. Chem. A* **2015**, *3*, 16988−16997.
(48) Snyder, R. L. The use of reference intensity ratios in X-ray quantitative analysis. *Powder Diffr.* **1992**, *7*, 186−193.
(49) Barpanda, P.; Ling, C. D.; Oyama, G.; Yamada, A. Sodium manganese fluorosulfate with a triplite structure. *Acta Crystallogr., Sect. B: Struct. Sci., Cryst. Eng. Mater.* **2013**, *69*, 584−588.
(50) Shannon, R. D. Revised effective ionic radii and systematic studies of interatomic distances in halides and chalcogenides. *Acta Crystallogr., Sect. A* **1976**, *32*, 751−767.
(51) Radha, A. V.; Subban, C. V.; Sun, M. L.; Tarascon, J. M.; Navrotsky, A. Possible correlation between enthalpies of formation and redox potentials in $LiMSO_4OH$ (M = Co, Fe, Mn) Li-ion polyanionic battery cathode materials. *J. Mater. Chem. A* **2014**, *2*, 6887−6894.
(52) Radha, A. V.; Furman, J. D.; Ati, M.; Melot, B. C.; Tarascon, J. M.; Navrotsky, A. Understanding the stability of fluorosulfate Li-ion battery cathode materials: a thermochemical study of $LiFe_{1-x}Mn_xSO_4F$ ($0 \le x \le 1$) polymorphs. *J. Mater. Chem.* **2012**, *22*, 24446−24452.

https://doi.org/10.1021/acs.chemmater.1c01669
Chem. Mater. 2021, 33, 6108−6119